Controllable Electrochemical Impedance Spectroscopy: From Circuit Design to Control and Data Analysis

Erfan Sadeghi, Mohammad Hosein Zand, Mohsen Hamzeh, Mehrdad Saif,
and Seyed Mohammad Mahdi Alavi

***Abstract*—This article describes fundamentals of controllable electrochemical impedance spectroscopy (cEIS), from circuit design to control and data analysis. In cEIS, a feedback system controls the process of injecting the excitation signal. We design a two degree-of-freedom robust control system, which guarantees tracking and stability of cEIS in the presence of model uncertainties. This article also addresses the concept of persistently exciting signals. cEIS using current driving mode (CDM) and voltage driving mode, and their differences are highlighted. An online cEIS device is designed and built based on the dc–dc buck converter for batteries online applications, where the excitation signal is superimposed on a dc level. The performance of the fabricated cEIS is evaluated through extensive experiments in CDM. The accuracy of the fabricated cEIS is tested, which results in 0.002 Ω root mean square error in the impedance spectra computation of a three-parameter Randles equivalent circuit model (ECM). The performance of the fabricated cEIS is practically verified on a battery cell at different C-rates. First-, second-, and fractional-order Randles ECMs are estimated by using system identification methods, and their impedance spectra are compared with those obtained through the fast Fourier transform.**

***Index Terms*—Batteries, electrochemical impedance spectroscopy (EIS), robust control, system identification.**

I. INTRODUCTION

ELECTROCHEMICAL impedance spectroscopy (EIS) has been a powerful tool for characterization, parameterization, and measurement of ohmic resistance, double layer capacitance, polarization, charge transfer, and diffusion processes in electrochemical systems [1], [2]. EIS is employed for fundamental research in cancer detection, [3]. It provides tools for prostate [4], breast [5], [6], and skin [7] cancers diagnosis. It has wide applications in neural engineering for noninvasive measurement of brain activities [8], and for *in vitro* and *in vivo* analysis of medical implants in deep brain stimulation [9], [10]. In energy systems, EIS is used for monitoring of energy storage systems such as batteries [1], supercapacitors [11], and fuel cells [12]. Several methods have been proposed for state-of-charge (SOC) estimation in electrochemical energy storage systems [13]–[15]. It has been shown that EIS can also be used for state-of-health (SOH) estimation such as computational analysis of aging effects [16], [17], degradation mechanisms [18], and internal temperature [19], [20] in electrochemical energy storage systems.

This article focuses on batteries EIS. In EIS, an excitation signal is injected into the battery, and its response is measured. If excitation signal is electric current, the voltage response is collected and vice versa. In [21], the excitation signal is electric current, generated by using a microcontroller and embedded digital-to-analog converter. However, the amplitude of the current signal is in the range of several hundred microamperes, which might not be sufficient to excite the battery cell. In [22] and [23], the EIS hardware is a bidirectional buck-boost dc–dc converter. In [22], a single-frequency sinusoidal signal is superimposed on the pulsewidth modulation (PWM) signal, which results in sinusoidal fluctuations on the battery current and voltage. The single-frequency sinusoidal signal is applied in an open-loop fashion. In [23], the excitation signal is a step-function perturbation, injected within a feedback control system. The application of triangular excitation current with feedback control, is studied in [24]. In [25], a switched-inductor ladder converter, with closed-loop control, is developed for cell balancing and EIS. In [25], impedance spectra are obtained by applying a random number of single-frequency sinusoidal current signals to the battery. The majority of EIS devices are based on the injection of a zero-mean excitation signal. As per [26] and [27], the excitation signal is superimposed on the charge or discharge current or voltage in this article, which makes it suitable for online applications. In [26], an online EIS device is designed based on dc-biased multisine and noise excitation currents generated by a motor controller. An integrated EIS

Manuscript received June 16, 2019; revised November 25, 2019; accepted February 20, 2020. Date of publication February 28, 2020; date of current version May 1, 2020. This work was supported by the Natural Sciences and Engineering Research Council of Canada NSERC. Recommended for publication by Associate Editor R. (GE) Zane. *(Corresponding author: Seyed Mohammad Mahdi Alavi.)*

Erfan Sadeghi and Mohammad Hosein Zand are with the Faculty of Electrical Engineering, Shahid Beheshti University, Tehran 1983969411, Iran (e-mail: erfan.sadeghi.work@gmail.com; hoseinzand.work@gmail.com).

Mohsen Hamzeh is with the School of Electrical and Computer Engineering, College of Engineering, University of Tehran, Tehran 1417466191, Iran (e-mail: mohsenhamzeh@ut.ac.ir).

Mehrdad Saif is with the Department of Electrical and Computer Engineering, University of Windsor, Windsor, ON N9B 3P4, Canada (e-mail: msaif@uwindsor.ca).

Seyed Mohammad Mahdi Alavi is with the Faculty of Electrical Engineering, Shahid Beheshti University, Tehran 1983969411, Iran, and also with the Department of Electrical and Computer Engineering, University of Windsor, Windsor, ON N9B 3P4, Canada (e-mail: m_alavi@sbu.ac.ir).

Color versions of one or more of the figures in this article are available online at http://ieeexplore.ieee.org.

Digital Object Identifier 10.1109/TPEL.2020.2977274

and high power battery charger is proposed in [27], based on a full-bridge phase shift-zero voltage switching dc–dc converter. In [27], a sweep signal with frequency range of 0.1–100 Hz is superimposed on the dc charging current, and impedance spectra of the battery are computed online by using the $d-q$ transformation.

In this article, we design a novel controllable EIS (cEIS) device, based on the dc–dc buck converter. A two degree-of-freedom (2DOF) robust control system is designed, based on quantitative feedback theory (QFT), for the control of the excitation signal [28], [29]. Other control methodologies are easily applicable with no need to redesign the hardware. Rarely, the battery model is considered in the design of EIS, [25], [27]. A feature of this article is to consider an integrated model of the converter and battery and their uncertainties into the control system design.

Batteries impedance spectra are mainly computed by using Fourier transform or its modified versions such as fast and discrete Fourier transforms, [21]–[24], [27]. Depending on the desired requirements, an equivalent circuit model (ECM) is fitted to the computed impedance spectra for quantitative analysis, [26], [30]. Since, we usually measure data in time-domain, novel EIS devices aim to directly estimate ECMs from time-domain measurements of current and voltage signals, and plot the impedance spectra of the ECM with no need to Fourier transforms [31], [32]. In the proposed cEIS, impedance spectra can be computed by both of these methods, using the fast Fourier transform (FFT) and system identification algorithms. For accurate estimation of ECMs, the current–voltage data should be informative. To this end, we also describe sufficient conditions that the excitation current signal should satisfy, in order to make sure that an informative dataset is achieved for cEIS. The effectiveness of the proposed cEIS is evaluated experimentally, and results are discussed. First-, second-, and fractional-order Randles ECMs are estimated by using system identification methods, and their impedance spectra are compared with those obtained through FFT.

A. Contributions of this Article

In summary, the main contributions of this work are highlighted as follows:

1) An online cEIS device, based on the dc–dc buck converter, is designed and tested experimentally. Both frequency- and time-domain techniques are used for the computation of the impedance spectra, and the results are compared.
2) A 2DOF robust control system based on QFT is designed, which guarantees stability and tracking of cEIS in the presence of model uncertainties.
3) The concept of persistently excitation is elaborated.

B. Outlines of this Article

In Section II, we describe the overall structure of a cEIS device. Differences between current and voltage modes cEIS are highlighted. The integration of cEIS to battery chargers is also manifested. In Section III, we elaborate the structure and design procedure of the robust control system. In Section IV, it is described how to choose the EIS excitation signal based on the concept of persistent excitation. In Section V, we test the fabricated cEIS in practice, and the results are discussed.

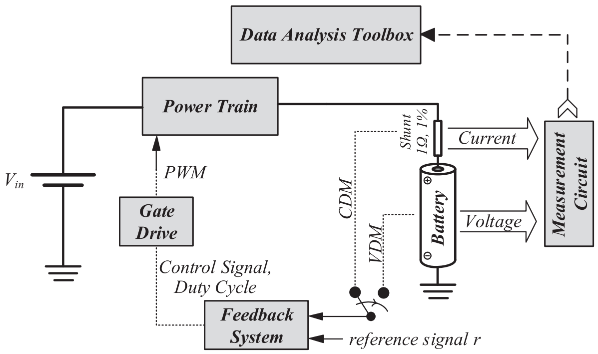

Fig. 1. Functional block diagram of batteries cEIS during the charge process.

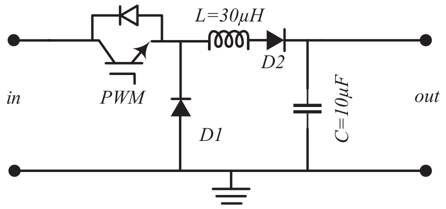

Fig. 2. Power train based on the DC-DC buck converter.

II. cEIS STRUCTURE, OVERALL OPERATION, AND SPECIFICATIONS

Fig. 1 shows a general functional block diagram of a cEIS device in battery systems engineering, during the charge process. It consists of five main parts: power supply V_{in}, power train, measurement circuit, feedback system, and data analysis toolbox. The power train converts the energy of the power supply V_{in} to a controllable excitation signal, superimposed on a dc level, and injects it to the battery. The operation of the power train is controlled by the feedback system. The battery's current and voltage data are transmitted to the data analysis toolbox for the computation of impedance spectra, ECMs, etc. Due to small amplitudes of excitation signals, a precision measurement circuit is required to appropriately filter and amplify the battery current and voltage. A central processing unit (CPU) is at the heart of the system for the implementation of the control systems, data acquisition, and analysis.

By the assumption that V_{in} is greater than the battery voltage, we design a buck-based power train, as shown in Fig. 2. The output LC filter of the converter with $L = 30\ \mu$H and $C = 10\ \mu$F results in a bandwidth of about $1/(2\pi\sqrt{LC}) = 9.1$ kHz, which is sufficient for batteries EIS applications, [26], [32]. The converter is operated at the switching frequency of 200 kHz. We employ the STMicroelectronics' STM32F4DISCOVERY kit as CPU, with the STM32F407VG microcontroller. The control signal is updated with a frequency of 20 kHz, which is sufficiently smaller than the converter's switching frequency. The continuous current and voltage signals, passing through the measurement circuit, are digitized with sampling frequency of

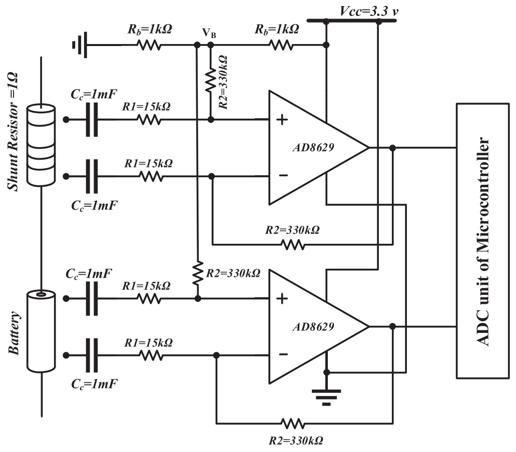

Fig. 3. Measurement circuit.

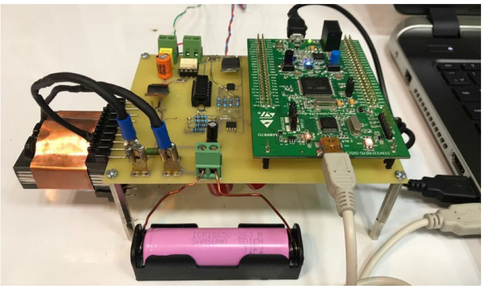

Fig. 4. Photograph of the fabricated cEIS device.

20 kHz by a 12-b analog-to-digital converter, which is embedded in the microcontroller. The digital data are sent to the computer via a full-speed 12Mb/s USB port for further process. The diode D2 is added in series with the inductor, in order to prevent the reverse current.

A. Measurement Circuit

Fig. 3 shows the designed measurement circuit. The capacitors C_c's remove the dc level, and operational amplifiers (op-amps) are set up in the differential amplifier mode, to accurately measure the EIS signals. The op-amps' dc-offset, V_B, is set to half of its supply voltage, in order to have the maximum swing, i.e., saturation limit. Precision shunt and measurement resistors, with 1% tolerance values, are used. Fig. 4 shows a photograph of the fabricated cEIS.

B. Current and Voltage Driving Modes cEIS

cEIS can be operated in current and voltage driving modes (CDM and VDM), where current and voltage excitation signals are controlled, respectively. Fundamentals of control system design and data analysis are exactly the same for both CDM and VDM. The only difference between them is the transfer function that is used for the control system design. In CDM, the transfer function from the PWM signal to the battery current is used. Whereas, the transfer function from the PWM signal to the battery voltage is utilized in VDM.

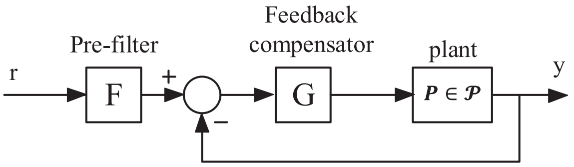

Fig. 5. Proposed 2DOF feedback control system.

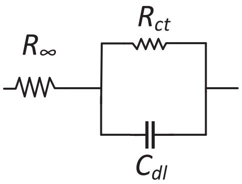

Fig. 6. First-order Randles ECM.

C. Integration of the Designed cEIS to Battery Chargers

The designed cEIS performs the charging and EIS tasks concurrently. In order to have a current-based charger, the cEIS is operated in CDM. Likewise, the VDM cEIS is in fact a voltage-based charger. In the chargers with mixed current-voltage control, e.g., constant-current constant-voltage (CCCV) battery chargers, cEIS switches between CDM and VDM modes.

D. cEIS During Discharge or Switching Between Charge and Discharge

For cEIS during discharge, V_{in} in Fig. 1 is replaced with the battery. The battery in Fig. 1 is replaced with a load. Fundamentals of control, selection of the excitation signal, and extraction of impedance spectra, which are presented in this article, remain unchanged. It is only required to alter the transfer function, according to the load's dynamics and operating modes CDM and VDM. For cEIS switching between charge and discharge, the power train has to be replaced with a bidirectional converter.

III. FEEDBACK SYSTEM DESIGN

Fig. 5 shows the structure of the proposed 2DOF feedback control system. The reference signal, r, is composed of the desired excitation current, r_{AC}, superimposed on the dc level, r_{DC}, as follows:

$$r = r_{\text{DC}} + r_{\text{AC}}. \tag{1}$$

The selection of r is discussed in Section IV. The plant P is an integrated model of the converter and battery in the uncertain region $\mathcal{P}$. The prefilter and feedback compensator, F and G, are designed such that the closed-loop system is stable and the battery current satisfactorily tracks the reference signal r for all plants in $\mathcal{P}$.

A. Integrated Model of the Converter and Battery

For the control system design, we use the first-order Randles ECM, as shown in Fig. 6, [33]. This model is widely used in EIS data analysis, [32], [33]. R_∞ is the ohmic resistor, R_{ct} represents the charge transfer resistance, and C_{dl} denotes the

TABLE I
UNCERTAINTY RANGE USED IN THE DESIGN

Parameter	Uncertainty Range
R_∞	[0.001, 0.3]Ω
R_{ct}	[0.001, 0.1]Ω
C_{dl}	[0.001, 100]F

double layer capacitance. The values of these parameters depend on the battery SOC and SOH. We design the control system for a wide range of uncertainty that is reported in the literature [32], [33]. The uncertainty region is given in Table I.

Let us assume that V_{in} is a well-rectified power supply. By using the averaging-method [34], an integrated state-space model of the converter and battery is derived as follows:

$$\begin{cases} \dot{x} = Ax(t) + Bd(t) \\ y(t) = Ex(t) \end{cases} \tag{2}$$

where $x = [i_L \quad v_C \quad v_{C_{dl}}]^T$ is the state vector, $d(t)$ is the control signal and the duty cycle of the PWM signal, and y is the battery current to be controlled. An uncertainty could also be considered on the inductor's value. By assuming internal resistances R_l and R_c for the inductor and output capacitor, the matrices of the state-space model are given by the following:

$$A = \begin{bmatrix} -\frac{R_s R_c + R_l(R_s+R_c)}{L(R_s+R_c)} & -\frac{R_s}{L(R_s+R_c)} & -\frac{R_c}{L(R_s+R_c)} \\ \frac{R_s}{C(R_s+R_c)} & -\frac{1}{C(R_s+R_c)} & \frac{1}{C(R_s+R_c)} \\ \frac{R_c}{C_{\text{dl}}(R_s+R_c)} & \frac{1}{C_{\text{dl}}(R_s+R_c)} & -\frac{(\frac{1}{R_s+R_c}+\frac{1}{R_{ct}})}{C_{\text{dl}}} \end{bmatrix}$$

$$B = \begin{bmatrix} \frac{V_{\text{in}}}{L} & 0 & 0 \end{bmatrix}^T, \quad E = \begin{bmatrix} \frac{R_c}{R_s+R_c} & \frac{1}{R_s+R_c} & -\frac{1}{R_s+R_c} \end{bmatrix}$$

and $R_s = R_\infty + R_{\text{shunt}}$

If the ripple of V_{in} is considerable, it is suggested to add a disturbance term in (2).

It is noted that the matrix E changes for the VDM cEIS as follows:

$$E = \begin{bmatrix} \frac{R_c R_\infty}{R_s+R_c} & \frac{R_\infty}{R_s+R_c} & \frac{R_{\text{shunt}}+R_c}{R_s+R_c} \end{bmatrix}.$$

The transfer function from d to y is simply calculated as follows:

$$P(s) = E(sI - A)^{-1}B. \tag{3}$$

where s is the Laplace operator.

The same averaging-based method is applicable for the derivation of the transfer functions in CDM and VDM cEIS during discharge.

B. Prefilter and Feedback Compensator Design

For the design of the prefilter and feedback compensator, the control objectives are first defined. In this work, robust stability and tracking performance are considered. For tracking performance, the prefilter and feedback compensator are designed such that the closed-loop response lies within an upper limit M_u, and a lower limit M_l, for all P's in the uncertain region $\mathcal{P}$, for the frequency range of interest. This is formulated as follows [28], [29]:

$$\left|M_l(j\omega)\right| \leq \left|H(j\omega)\right| \leq \left|M_u(j\omega)\right|$$
$$\text{for all } P \in \mathcal{P}, \text{ and } \omega \in \{\omega_{\text{tracking}}\}. \tag{4}$$

where

$$H(s) = F(s)\frac{P(s)G(s)}{1 + P(s)G(s)} \tag{5}$$

is the closed-loop transfer function from r to y. The tracking performance is computed for frequencies within the tracking bandwidth. The transfer functions of M_l and M_u are chosen, based on the desired specifications in terms of the settling time, overshoot, steady-state error, etc. The nature of the system is also important for the selection of M_u and M_l. We define M_u and M_l as follows, which aim to reach the steady state in about $10^{-4}(s)$, with maximum 10% overshoot.

$$M_u(s) = \frac{1}{\left(\frac{1}{62000^2}s^2 + \frac{1.2}{62000}s + 1\right)\left(\frac{1}{65000}s + 1\right)}$$

$$M_l(s) = \frac{1}{\left(\frac{1}{5000^2}s^2 + \frac{2}{5000}s + 1\right)\left(\frac{1}{6000}s + 1\right)}$$

The robust stability is satisfied by applying the following constraint:

$$\left|\frac{PG}{1 + PG}(j\omega)\right| \leq \gamma$$
$$\text{for all } P \in \mathcal{P}, \text{and } \omega \in \{\omega_{\text{stability}}\} \tag{6}$$

which guarantees the following gain and phase margins on the uncertainty region, [28], [29]

$$\text{G.M.} = 1 + 1/\gamma$$
$$\text{P.M.} = 180^\circ - 360\cos^{-1}(0.5/\gamma)/\pi.$$

The robust stability condition (6) is typically computed for frequencies above the tracking bandwidth. In this work, we choose $\gamma = 1.2$, which implies G.M.≈ 1.83 and P.M.$\approx 49.25^\circ$.

Disturbance rejection constraint can easily be added to the design. For instance, the following constraint is added for the rejection of the disturbance appearing at the input of the plant [28], [29]:

$$\left|\frac{P}{1 + PG}(j\omega)\right| \leq \left|W(j\omega)\right|$$
$$\text{for all } P \in \mathcal{P}, \text{ and } \omega \in \{\omega_{\text{dist-rejection}}\} \tag{7}$$

where W is the disturbance rejection weighting function.

The computation of (4), (6), and (7) results in a number of design bounds, which divide the Nichols chart into acceptable and unacceptable regions. The feedback compensator G is shaped such that the loop function

$$L_f(s) = P_o G(s) \tag{8}$$

lies within the acceptable region. In (8), P_o is a nominal plant, chosen from the uncertain region. It is shown that, QFT is robust to the selection of the nominal plant [29], thus we randomly choose the nominal plant. We compute the tracking bound (4)

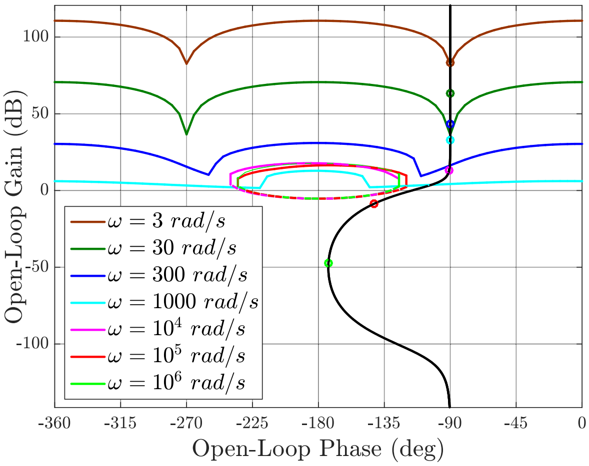

Fig. 7. Bounds for the design of the feedback compensator, and the loop-function, which satisfies all bounds.

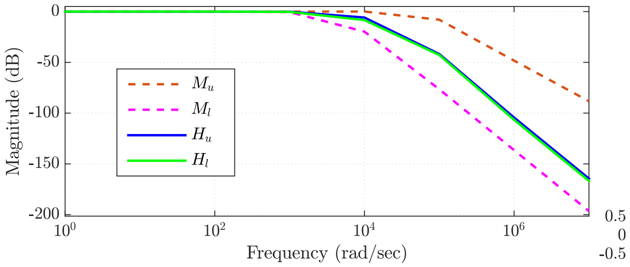

Fig. 8. Prefilter shaping in bode plot. M_u and M_l are the defined tracking limits. H_u and H_l denote the upper and lower responses of the closed-loop system, which are achieved by the designed $G(s)$ (9) and $F(s)$ (10).

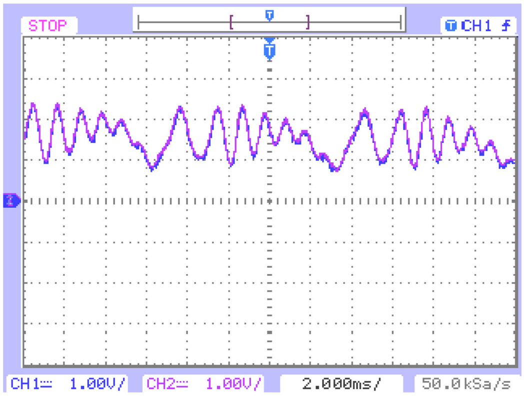

Fig. 9. Robust stability and tracking performance of the designed 2DOF. The reference signal r (Pink) is the summation of eight sinusoidal signals, with equal amplitudes 200 mA and frequencies $f = \{100, 200, 300, 400, 500, 600, 700, 800\}$Hz, superimposed on 1300 mA dc-level. The injected signal y (Blue) satisfactorily matches the reference signal r in the presence of parameters uncertainties.

for $\omega_{\text{tracking}} = [3, 30, 300, 1000]$(rad/s). We also compute the robust stability bound (6) for $\omega_{\text{stability}} = [10^4, 10^5, 10^6]$(rad/s). The intersection of the tracking and stability bounds is taken for the design of the feedback compensator. Fig. 7 shows the design bounds in the Nichols chart, computed by using the QFT toolbox [35]. The loop-function at each design frequency must lie above the associated solid lines, and below the dashed lines. The loop-function should also not enter the high-frequency stability contours. It is seen that the loop-function satisfies all design bounds by using the following proportional–integral compensator

$$G = \frac{0.113(s + 4.171 \times 10^4)}{s}. \tag{9}$$

The usage of the integral term improves the tracking performance at steady state, [36].

The prefilter F is designed by shaping the closed-loop system response $H(s)$ in bode plot. Fig. 8 shows that, by using the following prefilter:

$$F = \frac{1}{\frac{1}{60000}s + 1} \tag{10}$$

the closed-loop system response lies within the upper and lower limits M_u and M_l for all frequencies and uncertainties. In Fig. 8, H_u and H_l denote the upper and lower responses of the closed-loop system, which are achieved by the designed $G(s)$ and $F(s)$, i.e.,

$$\left|H_l(s)\right| \leq \left|H(s)\right| \leq \left|H_u(s)\right|$$
$$\text{with the designed } G(s) \text{ and } F(s) \text{ for all } P \in \mathcal{P}. \tag{11}$$

For the prefilter design in linear systems, it is sufficient to locate H_l and H_u between M_u and M_l.

For implementation in the microcontroller, the designed prefilter and feedback compensator are discretized by using the Tutsin transform, with control sampling rate of 20 kHz.

Fig. 9 shows the performance of the designed 2DOF control system on a Samsung's Li-ion battery cell ICR18650-26JM, with nominal voltage 3.63(V) and capacity 2.6(Ah). The reference signal r is the summation of eight sinusoidal signals superimposed on 1300 mA dc-level, which is equivalent to 0.5 C-rate of the battery. The magnitudes of the sinusoidal signals are equal to 200 mA, and their frequencies are $f = \{100, 200, 300, 400, 500, 600, 700, 800\}$Hz. As it is seen, the output current tracks the reference signal with a satisfactory level of robust stability and performance with respect to the unknown battery model. Small ripples on y are simply filtered in the data analysis toolbox, because the converter's switching frequency is known.

IV. SELECTION OF THE REFERENCE SIGNAL

This section describes the selection of the reference signal, $r(t)$, which consists of the EIS excitation signal r_{AC}, superimposed on a dc level r_{DC}. In order to have an informative dataset for EIS, the excitation signal r_{AC} should be persistently exciting of a proper order. A signal is said to be persistently exciting, if it appropriately excites the system's dynamics [37]. It is shown that if the order of persistent excitation equals the number of unknown parameters of the EIS model, an informative dataset is achieved [33]. For instance, there are three unknown parameters R_∞, R_{ct}, and C_{dl}, in the Randles ECM Fig. 6, thus, an excitation signal of order three is required for its model identification. Step function is persistently exciting of order one [37], thus it might not be a proper excitation signal for EIS. The multisine signal in the form of

$$r_{\mathrm{AC}}(t) = \sum_{j=1}^{l} m_j \sin(\omega_j t + \phi_j) \tag{12}$$

has received much attention for EIS, where l, is the number of sinusoids, and m_j, ω_j, and ϕ_j are the magnitude, frequency, and phase of the jth sinusoid, respectively, [26], [32], [33]. Each sinusoidal signal is persistently exciting of order two, thus, the multisine signal $r_{\mathrm{AC}}(t)$ is persistently exciting of order $2l$ provided that $\omega_j \neq 0 \neq \pi$, for all j's [37]. According to these statements, if the ECM has N unknown parameters, then, l in (12) should be chosen as follows in order to generate an informative data

$$l \geq \begin{cases} N/2, & \text{if } N \text{ is even} \\ (N+1)/2, & \text{if } N \text{ is odd.} \end{cases} \tag{13}$$

The phases ϕ_j's is in radian and can be any random value. However, if m_j's are equal, the Schroeder phase choice is suggested as follows, which reduces the Crest factor, a desired property of the signal waveform that is measured in system identification [37]

$$\phi_j = \begin{cases} \text{A random value}, & j = 1 \\ \phi_1 - \dfrac{j(j-1)}{l}\pi, & j \geq 2. \end{cases} \tag{14}$$

The magnitude of r is important for EIS. It should be chosen such that the battery works in the linear region. An empirical approach for the linearity check is to increase the amplitude of r until no frequency distortion is seen on the output. The higher the amplitude of r_{AC}, the better the EIS may achieve. Note that the noise level also affects the selection of m_j's. [37, Ch. 2] has provided more comprehensive information on the condition between the noise level and the system spectra. The gain of the measurement circuit may also require adequate tuning, in order to bring the signals' levels to the acceptable range. Finally, the dc level r_{DC} is chosen based on the desired C-rate and the amplitude of the excitation signal r_{AC}. Thus, an empirical tradeoff might be required between r_{AC} and r_{DC}.

V. EXPERIMENTAL RESULTS AND DISCUSSION

Several experimental tests are run in order to verify the performance of the designed cEIS.

A. *Test #1: Accuracy of the Designed cEIS*

This test is designed for the verification of the concept of persistent excitation. A first-order Randles circuit is built and connected to the cEIS device. We measured true values of the circuit components by using an *LCR* meter, and they are $R_\infty = 0.2199\ \Omega$, $R_{\mathrm{ct}} = 0.1108\ \Omega$, and $C_{\mathrm{dl}} = 0.0239$ F. According to (13), two summed-up sinusoidal signals are sufficient to achieve an informative dataset. The frequencies of sinusoids are arbitrarily chosen at 50 and 100 Hz. The phase of signals is selected by using the Schroeder phase choice (14). By using MATLAB SYSID toolbox [38], the parameters are estimated as follows: $R_{\infty,\mathrm{estimated}} = 0.2175\ \Omega$, $R_{\mathrm{ct,estimated}} = 0.1101\ \Omega$, and $C_{\mathrm{dl,estimated}} = 0.0243$ F. Fig. 10 shows the true and estimated impedance spectra of the first-order Randles ECMs. The root mean square error (RMSE) between the true and estimated impedance spectra Z^{true} and Z^{estimate}, is calculated as follows:

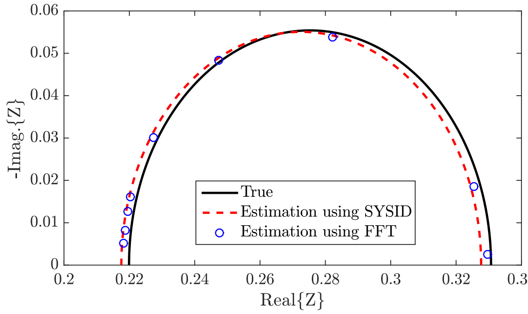

Fig. 10. Impedance spectra of the first-order Randles ECM obtained through tests #1 and #2.

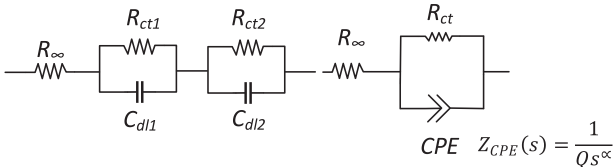

(a) (b)

Fig. 11. (a) Second- and (b) Fractional-order Randles ECMs.

$$\mathrm{RMSE} = \sqrt{\sum_{i=1}^{M} \frac{\left(\left|Z^{\mathrm{true}}_{f_i}\right| - \left|Z^{\mathrm{estimate}}_{f_i}\right|\right)^2}{M}} \tag{15}$$

where M denotes the number of sample points taken from the curves of impedance spectra for the RMSE calculation. Each sample point $i = 1, \ldots, M$ is associated with a certain frequency f_i. $|Z^{\mathrm{true}}_{f_i}|$ and $|Z^{\mathrm{estimate}}_{f_i}|$ are the magnitudes of the true and estimated impedance spectra at the sample point or frequency f_i, computed as follows:

$$\left|Z^{\mathrm{x}}_{f_i}\right| = \sqrt{(Re\{Z^{\mathrm{x}}\}_{f_i})^2 + (Im\{Z^{\mathrm{x}}\}_{f_i})^2}. \tag{16}$$

The superscript x represents the "true" and "estimate" terms. In this test, an RMSE of 0.0027 Ω, measured over nine sample points, was achieved between the true and estimated impedance spectra, which is quite satisfactory. This test demonstrates that a three-parameter first-order Randles ECM is accurately identifiable by using an excitation signal composed of two sinusoids.

B. *Test #2: Accuracy of the Designed cEIS*

This test is rerun in order to verify the FFT algorithm, which is employed in this work. A new excitation signal in the form of (12), composed of nine summed-up sinusoids within the range of 1 Hz up to 1 kHz is applied to the first-order Randles ECM test #1. The phase of the sinusoidal signals is selected by using the Schroeder phase choice (14). The impedance spectra obtained

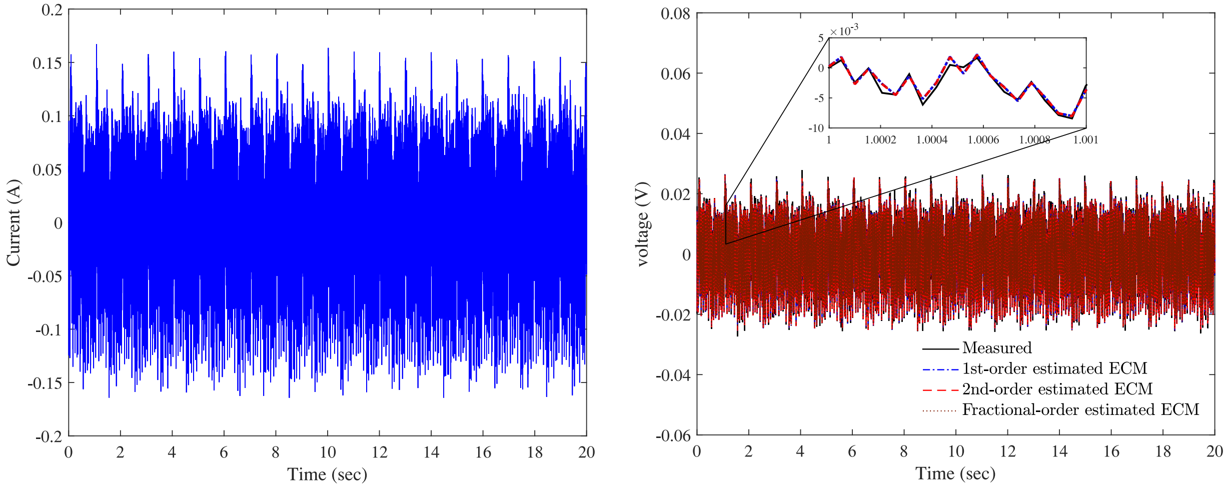

(a) (b)

Fig. 12. Measured time domain signals consisting of 21 summed-up sinuous used in the test #3. (a) Excitation current r_{AC}. (b) Response voltage.

from FFT are shown in Fig 10, which result in 0.0021 Ω RMSE, a bit smaller than that obtained from SYSID.

C. Test #3: Impact of C-Rate, Identification of First-, Second-, and Fractional-Order ECMs, and Comparison With FFT

A Samsung's ICR18650-26JM Li-ion battery cell with nominal voltage 3.63(V) and capacity 2.6(Ah) is tested using the fabricated cEIS device. An excitation current in the form of (12), consisting of 21 summed-up sinusoidal signals is applied to the battery at two different C-rates: 0.2 and 1 C-rates. Then, the impedance spectra of the battery are computed and plotted through both FFT and system identification methods. At 0.2C-rate the excitation current is superimposed on 0.5 A dc level. At 1C-rate, the excitation current is superimposed on 2.6 A dc level. The magnitudes of sinusoidal signals are equal to $m_j = 15$ mA, $j = 1, \ldots, 21$, with frequencies varying between 1 Hz and 2 kHz. The phase of signals is selected by using the Schroeder phase choice (14). Fig. 12 shows the excitation current and voltage response of the battery during the test at 0.2C-rate. DC levels are removed in Fig. 12 to highlight the superimposed fluctuations.

The first-, second-, and fractional-order Randles ECMs, shown, respectively, in Figs. 6 and 11 are identified by using the time-domain data and system identification methods. For the identification of the first- and second-order Randles ECMs, the MATLAB SYSID toolbox [38] is used. The fractional-order ECM is identified by using the proposed methodology in [32] and MATLAB CRONE toolbox [39]. Estimated values of the parameters are given in Table II.

Fig. 13 shows the impedance spectra, computed through the FFT and system identification methods for both 0.2 and 1 C-rates. Since FFT directly measures the impedance spectra, without the aid of modeling, we take it as the ground truth. Test #2 also confirmed the FFT's resolution. By using the RMSE formula (15), the error between the FFT's and first-order ECM's impedance spectra is 0.0011 Ω for test at 0.2C-rate, and 0.00066 Ω for test at 1C-rate. The errors between the FFT's impedance spectra, and those obtained via the second-order, and fractional-order ECMs is smaller as given in Table III. Thus, the second- and fractional-order ECMs result in more accurate estimations of the impedance spectra.

Fig. 13 also shows the impact of the C-rate on the impedance spectra. By increasing the charge rate, internal temperature of the battery increases, which in turn, facilitates the ionic movements, and reduces the internal impedance. This is clearly seen in Fig. 13 that the impedance spectra is shifted to the left in the Nyquist diagram and the parameters of the estimated ECMs, especially ohmic and charge transfer resistances, are

TABLE II
ESTIMATION OF THE FIRST-, SECOND-, AND FRACTIONAL-ORDER RANDLES ECMS PARAMETERS, BY USING THE SYSTEM IDENTIFICATION METHODS AT 0.2 AND 1 C-RATES

ECM	Parameter	0.2C-rate	1C-rate	
First-order	R_∞	0.1513	0.1388	Ω
	R_{ct}	0.0131	0.0084	Ω
	C_{dl}	0.2480	0.2760	F
Second-order	R_∞	0.1503	0.1380	Ω
	R_{ct1}	0.0083	0.0062	Ω
	C_{dl1}	0.1603	0.1810	F
	R_{ct2}	0.0071	0.0042	Ω
	C_{dl2}	1.4979	2.8333	F
Fractional-order	R_∞	0.1494	0.1365	Ω
	R_{ct}	0.0168	0.0124	Ω
	Q	0.6592	1.2381	F
	α	0.7967	0.6905	$Fcm^{-2}s^{\alpha-1}$

TABLE III
RMSE BETWEEN THE IMPEDANCE SPECTRA OF FFT AND THOSE ESTIMATED THROUGH RANDLES ECMS BY USING (15)

	0.2C-rate	1C-rate
FFT vs. first-order ECM	0.0011 Ω	0.00066 Ω
FFT vs. second-order ECM	0.00046 Ω	0.00021 Ω
FFT vs. fractional-order ECM	0.00070 Ω	0.00034 Ω

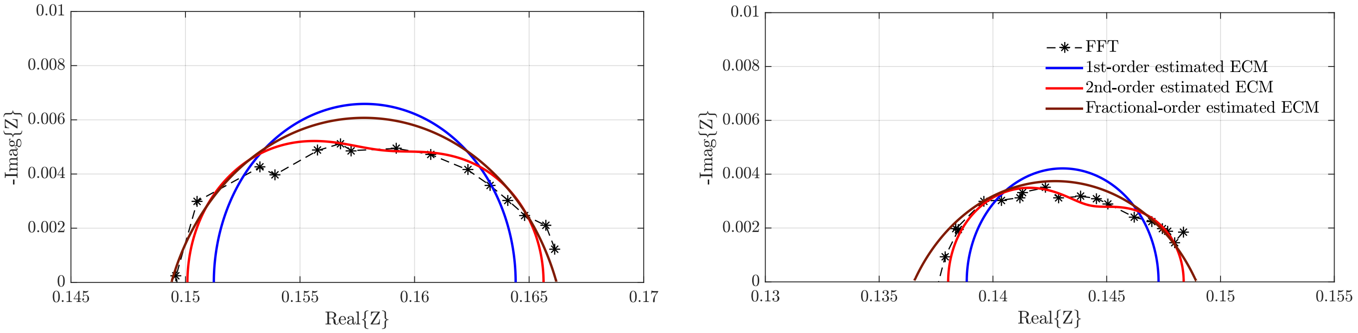

(a) (b)

Fig. 13. Impedance spectra of the battery in test #3, computed by using FFT, and identification of the first, second, and fractional-order Randles ECMs. (a) 0.2 C-rate. (b) 1 C-rate.

significantly decreased at 1C-rate compared to 0.2C-rate. These results confirm the literature [40], [41].

The voltage responses of the identified ECMs are plotted in Fig. 12(b), which are very close to the measured voltage, with RMSEs around 0.0008 V. This test illustrates that a good fit in the time domain does not necessarily lead to the correct estimation of impedance spectra in the Nyquist diagram. Further research is required to study the map between the estimations in time and frequency domains. Direct estimation of EIS models by fitting to the impedance spectra in the Nyquist diagram, and evaluation of the voltage response of the resulting EIS model might help to address this issue.

VI. CONCLUSION

In this article, a novel cEIS device was developed by using the dc–dc buck converter. A feature of cEIS is to control tracking and stability of injecting the excitation signal in a closed-loop fashion, in the presence of model uncertainties. This article has focused on CDM cEIS during charging process. We also addressed the development of cEIS to VDM and discharge processes. The dynamics of the power train and battery, both have been considered into the control system design. In this work, we designed a robust control system based on the 2DOF feedback structure. Other control techniques can be applied without hardware change. Extensive experimental tests were run to verify the effectiveness of the fabricated cEIS. Both time and frequency domains approaches were used for the computation of impedance spectra. We evaluated the performance of first-, second-, and fractional-order Randles ECMs. We experimentally demonstrated that the selection of an excitation signal by using the concept of persistent excitation results in a RMSE around 0.002 Ω in the identification of three-parameter Randles ECM. We also showed that the distance between the impedance spectra generated by FFT and those generated by the second- and fractional order Randles ECMs is significantly smaller than the distance between the impedance spectra generated by FFT and those generated by the first-order Randles ECM. We also verified the performance of fabricated cEIS at different C-rates.

As a future research, development of a cEIS with bidirectional power train is suggested, which can switch between both charge and discharge processes. Development of diagnosis methods by using the designed cEIS, and investigation of the map between the EIS model identification in frequency and time domains are also suggested for future research.

ACKNOWLEDGMENT

The authors would like to thank the editors and anonymous reviewers for their constructive inputs and comments, which improved the quality of this article.

REFERENCES

[1] E. Barsoukov and J. R. Macdonald, *Impedance Spectroscopy: Theory, Experiment, and Applications*. Hoboken, NJ, USA: Wiley, 2005.

[2] D. A. Howey and S. M. M. Alavi, "Rechargeable battery energy storage system design," *Handbook Clean Energy Systems*, J. Yan, vol. 5, ed., Hoboken, NJ, USA: Wiley, 2015, pp. 2801–2818.

[3] R. Wang, J. Di, J. Ma, and Z. Ma, "Highly sensitive detection of cancer cells by electrochemical impedance spectroscopy," *Electrochim. Acta*, vol. 61, pp. 179–184, 2012.

[4] V. Mishra, H. Bouayad, A. Schned, A. Hartov, J. Heaney, and R. J. Halter, "A real-time electrical impedance sensing biopsy needle," *IEEE Trans. Biomed. Eng.*, vol. 59, no. 12, pp. 3327–3336, Dec. 2012.

[5] Z. Haeri, M. Shokoufi, M. Jenab, R. Janzen, and F. Golnaraghi, "Electrical impedance spectroscopy for breast cancer diagnosis: Clinical study," *Integrative Cancer Sci. Therapeutics*, vol. 3, no. 6, pp. 1–6, 2016.

[6] T.-J. Kao *et al.*, "Regional admittivity spectra with tomosynthesis images for breast cancer detection: Preliminary patient study," *IEEE Trans. Med. Imag.*, vol. 27, no. 12, pp. 1762–1768, Dec. 2008.

[7] R. P. Braun, J. Mangana, S. Goldinger, L. French, R. Dummer, and A. A. Marghoob, "Electrical impedance spectroscopy in skin cancer diagnosis," *Dermatol. Clin.*, vol. 35, no. 4, pp. 489–493, 2017.

[8] G. Besancon, G. Becq, and A. Voda, "Fractional-order modeling and identification for a phantom EEG system," *IEEE Trans. Control Syst. Technol.*, vol. 28, no. 1, pp. 130–138, Jan. 2020.

[9] S. F. Lempka, S. Miocinovic, M. D. Johnson, J. L. Vitek, and C. C. McIntyre, "In vivo impedance spectroscopy of deep brain stimulation electrodes," *J. Neural Eng.*, vol. 6 no. 4, 2009, Art. no. 046001.

[10] A. Mercanzini, P. Colin, J.-C. Bensadoun, A. Bertsch, and P. Renaud, "In vivo electrical impedance spectroscopy of tissue reaction to microelectrode arrays," *IEEE Trans. Biomed. Eng.*, vol. 56, no. 7, pp. 1909–1918, 2009.

[11] S. Buller, M. Thele, R. De Doncker, and E. Karden, "Impedance-based simulation models of supercapacitors and Li-ion batteries for power electronic applications," *IEEE Trans. Ind. Appl.*, vol. 41, no. 3, pp. 742–747, May/Jun. 2005.

[12] C. de Beer, P. S. Barendse, and P. Pillay, “Fuel cell condition monitoring using optimized broadband impedance spectroscopy,” *IEEE Trans. Ind. Electron.*, vol. 62, no. 8, pp. 5306–5316, Aug. 2015.

[13] H. Blanke *et al.*, “Impedance measurements on leadacid batteries for state-of-charge, state-of-health and cranking capability prognosis in electric and hybrid electric vehicles,” *J. Power Sources*, vol. 144, no. 2, pp. 418–425, 2015.

[14] Y. Ma, X. Zhou, B. Li, and H. Chen, “Fractional modeling and SOC estimation of lithium-ion battery,” *IEEE/CAA J. Automat. Sinica*, vol. 3, no. 3, pp. 281–287, 2016.

[15] R. Xiong, J. Tian, W. Shen, and F. Sun, “A novel fractional order model for state of charge estimation in lithium ion batteries,” *IEEE Trans. Veh. Technol.*, vol. 68, no. 5, pp. 4130–4139, May 2019.

[16] A. Guha and A. Patra, “Online estimation of the electrochemical impedance spectrum and remaining useful life of lithium-ion batteries,” *IEEE Trans. Instrum. Meas.*, vol. 67, no. 8, pp. 1836–1849, Aug. 2018.

[17] U. Tröltzsch, O. Kanoun, and H.-R. Tränkler, “Characterizing aging effects of lithium ion batteries by impedance spectroscopy,” *Electrochimica Acta*, vol. 51, no. 8, pp. 1664–1672, 2006.

[18] J. Tian, R. Xiong, and Q. Yu, “Fractional-order model-based incremental capacity analysis for degradation state recognition of lithium-ion batteries,” *IEEE Trans. Ind. Electron.*, vol. 66, no. 2, pp. 1576–1584, Feb. 2019.

[19] R. R. Richardson, P. T. Ireland, and D. A. Howey, “Battery internal temperature estimation by combined impedance and surface temperature measurement,” *J. Power Sources*, vol. 265, pp. 254–261, 2014.

[20] J. G. Zhu, Z. C. Sun, X. Z. Wei, and H. F. Dai, “A new lithium-ion battery internal temperature on-line estimate method based on electrochemical impedance spectroscopy measurement,” *J. Power Sources*, vol. 274, pp. 990–1004, 2015.

[21] S. Grassini, S. Corbellini, and E. Angelini, “Low-cost impedance spectroscopy system based on a logarithmic amplifier,” *IEEE Trans. Instrum. Meas.*, vol. 64, no. 5, pp. 1110–1117, May 2015.

[22] W. Huang and J. A. Abu Qahouq, “An online battery impedance measurement method using DC-DC power converter control,” *IEEE Trans. Ind. Electron.*, vol. 61, no. 11, pp. 5987–5995, Nov. 2014.

[23] J. A. Abu Qahouq and Z. Xia, “Single-perturbation-cycle online battery impedance spectrum measurement method with closed-loop control of power converter,” *IEEE Trans. Ind. Electron.*, vol. 64, no. 9, pp. 7019–7029, Sep. 2017.

[24] L. Zhang, Z. Zhou, Q. Chen, R. Long, and S. Quan, “Model predictive control for electrochemical impedance spectroscopy measurement of fuel cells based on neural network optimization,” *IEEE Trans. Transp. Electrif.*, vol. 5, no. 2, pp. 524–534, Jun. 2019.

[25] E. Din, C. Schaef, K. Moffat, and J. T. Stauth, “A scalable active battery management system with embedded real-time electrochemical impedance spectroscopy,” *IEEE Trans. Power Electron.*, vol. 32, no. 7, pp. 5688–5698, Jul. 2017.

[26] D. A. Howey, P. D. Mitcheson, V. Yufit, G. J. Offer, and N. P. Brandon, “Online measurement of battery impedance using motor controller excitation,” *IEEE Trans. Veh. Technol.*, vol. 63, no. 6, pp. 2557–2566, Jul. 2014.

[27] Y.-D. Lee, S.-Y. Park, and S.-B. Han, “Online embedded impedance measurement using high-power battery charger,” *IEEE Trans. Ind. Appl.*, vol. 51, no. 1, pp. 498–508, Jan. 2015.

[28] S. M. M. Alavi and M. Saif, “A QFT-based decentralized design approach for integrated fault detection and control,” *IEEE Trans. Control Syst. Technol.*, vol. 20, no. 5, pp. 1366–1375, Sep. 2012.

[29] C. H. Houpis, S. J. Rasmussen, and M. Garcia-Sanz, *Quantitative Feedback Theory: Fundamentals and Applications*, 2nd ed., Boca Raton, FL, USA: CRC Press, Dec. 2005.

[30] J. Sabatier, J. M. Francisco, F. Guillemard, L. Lavigne, M. Moze, and M. Merveillaut, “Lithium-ion batteries modeling: A simple fractional differentiation based model and its associated parameters estimation method,” *Signal Process.*, vol. 107, pp. 290–301, 2015.

[31] P. E. Jacob, S. M. M. Alavi, A. Mahdi, S. J. Payne, and D. A. Howey, “Bayesian inference in non-Markovian state-space models with applications to battery fractional-order systems,” *IEEE Trans. Control Syst. Technol.*, vol. 26, no. 2, pp. 497–506, Mar. 2018.

[32] S. M. M. Alavi, C. R. Birkl, and D. A. Howey, “Time-domain fitting of battery electrochemical impedance models,” *J. Power Sources*, vol. 288, pp. 345–352, 2015.

[33] S. M. M. Alavi, A. Mahdi, S. J. Payne, and D. A. Howey, “Identifiability of generalised Randles circuit models,” *IEEE Trans. Control Syst. Technol.*, vol. 25, no. 6, pp. 2112–2120, Nov. 2017.

[34] R. D. Middlebrook and S. Cuk, “A general unified approach to modelling switching-converter power stages,” in *Proc. IEEE Power Electron. Specialists Conf.*, Jun. 1976, pp. 73–86.

[35] M. Garcia-Sanz, *The QFT Control Toolbox (QFTCT) for Matlab*, 2008.

[36] B. Labibi and S. M. M. Alavi, “Inversion-free decentralised quantitative feedback design of large-scale systems,” *Int. J. Syst. Sci.*, vol. 47, no. 8, pp. 1772–1782, 2006.

[37] L. Ljung, “System identification: Theory for the user,” *PTR Prentice Hall Information and System Sciences Series*. Englewood Cliffs, NJ, USA: Prentice-Hall, vol. 198, 1987.

[38] L. Ljung, *System Identification Toolbox for Use With MATLAB*. Natick, MA, USA: MathWorks, 1988.

[39] A. Oustaloup, P. Melchior, P. Lanusse, O. Cois, and F. Dancla, “The CRONE toolbox for Matlab,” in *Proc. IEEE Int. Symp. Comput.-Aided Control System Des.*, 2000, pp. 190–195.

[40] D. Stroe, V. Knap, M. Swierczynski, and E. Schaltz, “Electrochemical impedance spectroscopy-based electric circuit modeling of lithium-sulfur batteries during a discharging state,” *IEEE Trans. Industry Appl.*, vol. 55, no. 1, pp. 631–637, Jan./Feb. 2019.

[41] Q. Wang, Y. He, J. Shen, and X. Hu, “State of charge dependent polynomial equivalent circuit modeling for electrochemical impedance spectroscopy of lithium-ion batteries,” *IEEE Trans. Power Electron.*, vol. 33, no. 10, pp. 631–637, Oct. 2018.

Erfan Sadeghi received the B.A.Sc. degrees in electrical engineering from Urmia University, Urmia, Iran, in 2016, and the M.A.Sc. degree from Shahid Beheshti University, Tehran, Iran, in 2020.

His research interests include the design and development of power electronics and control systems for transportation electrification, renewable energies, and energy storage systems.

Mohammad Hosein Zand received the B.A.Sc. degree in electrical engineering from the Qom University of Technology, Qom, Iran, in 2017. He is currently working toward the M.A.Sc. degree with Shahid Beheshti University, Tehran, Iran.

His research interests include battery systems diagnostics, EVs’ charge stations, energy storage systems in renewable energies, and application of control systems in power electronics.

Mohsen Hamzeh received the B.Sc. and M.Sc. degrees from the University of Tehran, Tehran, Iran, in 2006 and 2008, respectively, and the Ph.D. degree from Sharif University of Technology, Tehran, Iran, in 2012, all in electrical engineering.

From 2013 to 2018, he was an Assistant Professor with Shahid Beheshti University, Tehran, Iran. In 2018, he joined the School of Electrical and Computer Engineering, University of Tehran. His research interests include renewable energies, microgrid control and applications of power electronics in power distribution systems.

Mehrdad Saif received the B.S.E.E, M.S.E.E, and D.Eng. degrees from Cleveland State University, Cleveland, OH, USA, in 1982, 1984, and 1987, respectively.

During his graduate studies, he worked on research projects sponsored by NASA Lewis (now Glenn) Research Center, as well as Cleveland Advanced Manufacturing Program (CAMP). In 1987, he joined the School of Engineering Science, Simon Fraser University, as an Assistant Professor. From 2002 to 2011, he was the Director of the School of Engineering Science, and led major expansion of that School during his term. He has been the Dean of the Faculty of Engineering with the University of Windsor, since July 2011. In this role, he has led major enrollment growth through strategic enrollment management and the expansion of Faculty of Engineering programs into areas of aerospace engineering, engineering management, B.Eng. technology, mechatronics, and others. He has also overseen significant growth in the number of Faculty as well as research productivity of the Faculty of Engineering. He was a Consultant to a number of industries and agencies such as GM, NASA, B.C. Hydro, Ontario Council of Graduate Studies, and others. He has authored or coauthored about 350 refereed journal and conference papers plus an edited book in these areas. His research interests include systems and control, estimation and observer theory, model-based fault diagnostics, condition monitoring, diagnostics and prognostic, and application of these areas to automotive, power, autonomous systems, and other complex and cyber-physical systems.

Dr. Saif has served two terms (1995, 1997) as the Chairman of the Vancouver Section of the IEEE Control Systems Society, and is currently a member of the Editorial Board of IEEE Access, and the IEEE SYSTEMS JOURNAL. He is a Registered Professional Engineer in Ontario, Canada, and is a Fellow of the Canadian Academy of Engineering (CAE) as well as the Institution of Engineering and Technology (IET).

Seyed Mohammad Mahdi Alavi received the B.A.Sc. and M.A.Sc. degrees from K. N. Toosi University of Technology, Tehran, Iran, in 2001 and 2003, respectively, and the Ph.D. degree from the University of Limerick, Limerick, Ireland, in 2009.

He worked as a Researcher with Simon Fraser University from 2009 to 2011, the University of Windsor from 2011 to 2014, the University of Oxford from 2014 to 2015, Duke University from 2015 to 2016, and the University of Calgary from 2016 to 2017. Since April 2017, he has been an Assistant Professor with the Faculty of Electrical Engineering, Shahid Beheshti University, Tehran, Iran. Since July 2019, he has been on sabbatical leave, visiting the University of Windsor, and University of British Columbia.

His research interests include the design and development of condition monitoring, control, and (power) electronic systems for battery systems and noninvasive brain stimulation engineering through transcranial magnetic stimulation (TMS). In the field of battery systems engineering, he has contributed to the development of condition monitoring and control systems and devices for efficient and robust battery testing and diagnostics, power conversion and charging systems, and grid integration. In the field of TMS, he has contributed to the design and development of integrated hardware and software systems for modeling and estimation of neural recruitment or input–output (IO) curves. He is a Designer and Developer of TMS ioFit, an open-source MATLAB-based toolbox for fast, accurate, and closed-loop identification of TMS IO curves, based on sequential parameter estimation methods and Fisher's principles.